Draft version December 2, 2022
Typeset using LaTeX **twocolumn** style in AASTeX631

arXiv:2212.00130v1 [astro-ph.GA] 30 Nov 2022

PHANGS-JWST First Results: The Influence of Stellar Clusters on PAHs in Nearby Galaxies

Daniel A. Dale,[1] Médéric Boquien,[2] Ashley T. Barnes,[3] Francesco Belfiore,[4] F. Bigiel,[3] Yixian Cao,[5] Rupali Chandar,[6] Jérémy Chastenet,[7] Mélanie Chevance,[8,9] Sinan Deger,[10] Oleg V. Egorov,[11] Kathryn Grasha,[12,13] Brent Groves,[14] Hamid Hassani,[15] Kiana F. Henny,[1] Ralf S. Klessen,[8,16] Kathryn Kreckel,[11] J. M. Diederik Kruijssen,[9] Kirsten L. Larson,[17] Janice C. Lee,[18] Adam K. Leroy,[19] Daizhong Liu,[5] Eric J. Murphy,[20] Erik Rosolowsky,[15] Karin Sandstrom,[21] Eva Schinnerer,[22] Jessica Sutter,[21] David A. Thilker,[23] Elizabeth J. Watkins,[11] Bradley C. Whitmore,[24] and Thomas G. Williams[25,22]

[1] *Department of Physics and Astronomy, University of Wyoming, Laramie, WY 82071, USA*
[2] *Centro de Astronomía (CITEVA), Universidad de Antofagasta, Avenida Angamos 601, Antofagasta, Chile*
[3] *Argelander-Institut für Astronomie, Universität Bonn, Auf dem Hügel 71, 53121, Bonn, Germany*
[4] *INAF — Arcetri Astrophysical Observatory, Largo E. Fermi 5, I-50125, Florence, Italy*
[5] *Max-Planck-Institut für Extraterrestrische Physik (MPE), Giessenbachstr. 1, D-85748 Garching, Germany*
[6] *Ritter Astrophysical Research Center, University of Toledo, Toledo, OH 43606, USA*
[7] *Sterrenkundig Observatorium, Universiteit Gent, Krijgslaan 281 S9, B-9000 Gent, Belgium*
[8] *Institut für Theoretische Astrophysik, Zentrum für Astronomie der Universität Heidelberg, Albert-Ueberle-Strasse 2, 69120 Heidelberg, Germany*
[9] *Cosmic Origins Of Life (COOL) Research DAO, coolresearch.io*
[10] *TAPIR, California Institute of Technology, Pasadena, CA 91125 USA*
[11] *Astronomisches Rechen-Institut, Zentrum für Astronomie der Universität Heidelberg, Mönchhofstr. 12-14, D-69120 Heidelberg, Germany*
[12] *Research School of Astronomy and Astrophysics, Australian National University, Canberra, ACT 2611, Australia*
[13] *ARC Centre of Excellence for All Sky Astrophysics in 3 Dimensions (ASTRO 3D), Australia*
[14] *International Centre for Radio Astronomy Research, University of Western Australia, 35 Stirling Highway, Crawley, WA 6009, Australia*
[15] *Department of Physics, University of Alberta, Edmonton, AB T6G 2E1, Canada*
[16] *Universität Heidelberg, Interdisziplinäres Zentrum für Wissenschaftliches Rechnen, Im Neuenheimer Feld 205, D-69120 Heidelberg, Germany*
[17] *AURA for the European Space Agency (ESA), Space Telescope Science Institute, 3700 San Martin Drive, Baltimore, MD 21218, USA*
[18] *Gemini Observatory/NSF NOIRLab, 950 N. Cherry Avenue, Tucson, AZ 85719, USA*
[19] *Department of Astronomy, The Ohio State University, 140 West 18th Ave., Columbus, OH 43210, USA*
[20] *National Radio Astronomy Observatory, 520 Edgemont Road, Charlottesville, VA 22903, USA*
[21] *Center for Astrophysics & Space Sciences, Department of Physics, University of California San Diego, 9500 Gilman Drive, La Jolla, CA 92093, USA*
[22] *Max Planck Institut für Astronomie, Königstuhl 17, 69117 Heidelberg, Germany*
[23] *Department of Physics and Astronomy, The Johns Hopkins University, Baltimore, MD 21218 USA*
[24] *Space Telescope Science Institute, 3700 San Martin Drive, Baltimore, MD 21218, USA*
[25] *Sub-department of Astrophysics, Department of Physics, University of Oxford, Keble Road, Oxford OX1 3RH, UK*

ABSTRACT

We present a comparison of theoretical predictions of dust continuum and polycyclic aromatic hydrocarbon (PAH) emission with new JWST observations in three nearby galaxies: NGC 628, NGC 1365, and NGC 7496. Our analysis focuses on a total of 1063 compact stellar clusters and 2654 stellar associations previously characterized by HST in the three galaxies. We find that the distributions and trends in the observed PAH-focused infrared colors generally agree with theoretical expectations, and that the bulk of the observations is more aligned with models of larger, ionized PAHs. These JWST data usher in a new era of probing interstellar dust and studying how the intense radiation fields near stellar clusters and associations play a role in shaping the physical properties of PAHs.

1. INTRODUCTION

Corresponding author: Daniel A. Dale
ddale@uwyo.edu

Polycyclic aromatic hydrocarbon (PAHs) contribute as much as 20% of a star-forming galaxy's total infrared emission (Smith et al. 2007) and produce bright emission features in the mid-infrared (e.g., Tielens 2008) that have been used as star formation tracers across cosmic time (e.g., Riechers et al. 2014). However, PAH emission exhibits large variability within and between galaxies, and it is important to determine the factors that drive PAH properties and strength. Previous studies of PAH emission features in galaxies have shown that the strength of PAH emission is sensitive to the metal abundance of the interstellar medium, the molecular gas surface density, the hardness and strength of the interstellar radiation field (or related metrics such as the star formation rate, dust temperature, active galactic nucleus X-ray luminosity, etc.), or some combination thereof (e.g., Engelbracht et al. 2005; Madden et al. 2006; Wu et al. 2006; Draine et al. 2007; Engelbracht et al. 2008; Dale et al. 2009; Sandstrom et al. 2010; Wu et al. 2010; Rémy-Ruyer et al. 2015; Jensen et al. 2017; Chastenet et al. 2019; Aniano et al. 2020; Galliano et al. 2021; Wolfire et al. 2022). These studies that were completed using previous generations of space-based infrared facilities targeted bright peaks of infrared emission or averaged over large swaths of lower surface brightness regions. The advent of the more sensitive instruments aboard JWST enable characterization of the PAH emission at high angular resolution across entire galaxy disks, including the 3.3 μm PAH feature which is essential to constraining the PAH size distribution but heretofore rarely observed for statistically significant samples (Lai et al. 2020, and references therein). Similarly, the relative strengths of PAH emission features, including those at 3.3, 7.7, and 11.2 μm, have long been thought to be critically dependent on the levels of PAH ionization (e.g., DeFrees & Miller 1989; Allamandola et al. 1999).

With JWST and HST we present a novel study of the relationship between the strength of three key PAH mid-infrared features on the physical scales of star clusters and associations, and investigate trends with the ages of those stellar populations. Intense ultraviolet radiation from star clusters dominated by young OB stars will, for example, ionize or even destroy PAHs, which in turn will impact the local reddening curve, the efficiency of the heating of the neutral interstellar medium, chemical reaction rates, etc. (Hollenbach & Tielens 1997; Draine et al. 2007; Tielens 2008; Wolfire et al. 2022). We compare the theoretical predictions for PAH emission features with photometric observations from JWST for the Physics at High Angular resolution in Nearby GalaxieS (PHANGS) program on nearby galaxies (Leroy et al. 2021; Emsellem et al. 2022; Lee et al. 2022b,a), using three filters with bandpasses that capture PAH emission features centered at 3.3, 7.7, and 11.2 μm. We specifically compare our observations with the predictions laid out in Draine et al. (2021) (see also Rigopoulou et al. 2021) for a range of PAH ionization levels and size distributions in addition to a variety of interstellar radiation field intensities and ages of the stellar populations that drive the dust heating.

2. SAMPLE AND DATA

The galaxies and observations analyzed here are drawn from the PHANGS project. The first wave of PHANGS–JWST data included a suite of NIRCam (Rieke et al. 2005) and MIRI (Rieke et al. 2015) imaging for three star-forming galaxies. NGC 628 is a grand-design spiral galaxy at 9.84 Mpc, and both NGC 1365 (19.57 Mpc) and NGC 7496 (18.72 Mpc) are barred spirals with Seyfert nuclei (distances are from Shaya et al. 2017; Kourkchi & Tully 2017; Anand et al. 2021a,b). The NIRCam mosaics use the F200M, F300M, F335M, and F360M filters and the MIRI mosaics use the F770W, F1000W, F1130W, and F2100W filters. The technical description and post-processing of the NIRCam and MIRI imaging for the PHANGS-JWST program is described in Lee et al. (2022a).

The catalog of stellar clusters utilized here is from the PHANGS–HST program (Turner et al. 2021; Lee et al. 2022b; Thilker et al. 2022); we restrict our analysis to the Class 1 and 2 clusters (Whitmore et al. 2021; Deger et al. 2022) which are either compact and centrally concentrated (Class 1) or compact and slightly asymmetric (Class 2). In lieu of using the catalog of asymmetric and multi-peaked Class 3 stellar associations, which is comparatively incomplete since the PHANGS–HST pipeline was optimized for detecting single-peaked compact clusters, we utilize the PHANGS–HST catalog of stellar associations. These stellar associations, which are less likely to be gravitationally bound than Class 1 and 2 compact clusters (Whitmore et al. 2021), are derived from a watershed analysis that is based on V-band point-source detections and a 32 pc full-width-half-maximum Gaussian smoothing, as presented in (Lee et al. 2022a) and Larson et al. (in prep). The stellar masses and ages for the clusters and associations are based on spectral energy distribution fits to the five-band ultraviolet/optical PHANGS–HST datasets and span $\sim 10^{2.8-7.0}$ $M_\odot$ and 1 Myr to 13 Gyr (see also Turner et al. 2021).

There are a total of $330 + 501 + 232 = 1063$ compact clusters and $1539 + 689 + 426 = 2654$ stellar associations in the publicly-available catalogs that overlap with the PHANGS–JWST footprints for NGC 628, NGC 1365, and NGC 7496, respectively. As can be seen in Figure 1, these three galaxies are rich with mid-infrared emission throughout their disks; 95% of the compact clusters and 93% of the stellar associations show mid-infrared emission coincident with their locations in at least one of the three bandpasses.

We remove clusters and associations for which their mid-infrared photometry is potentially impacted by the saturation effects associated with the active galactic nuclei for NGC 1365 and NGC 7496. Following Hassani

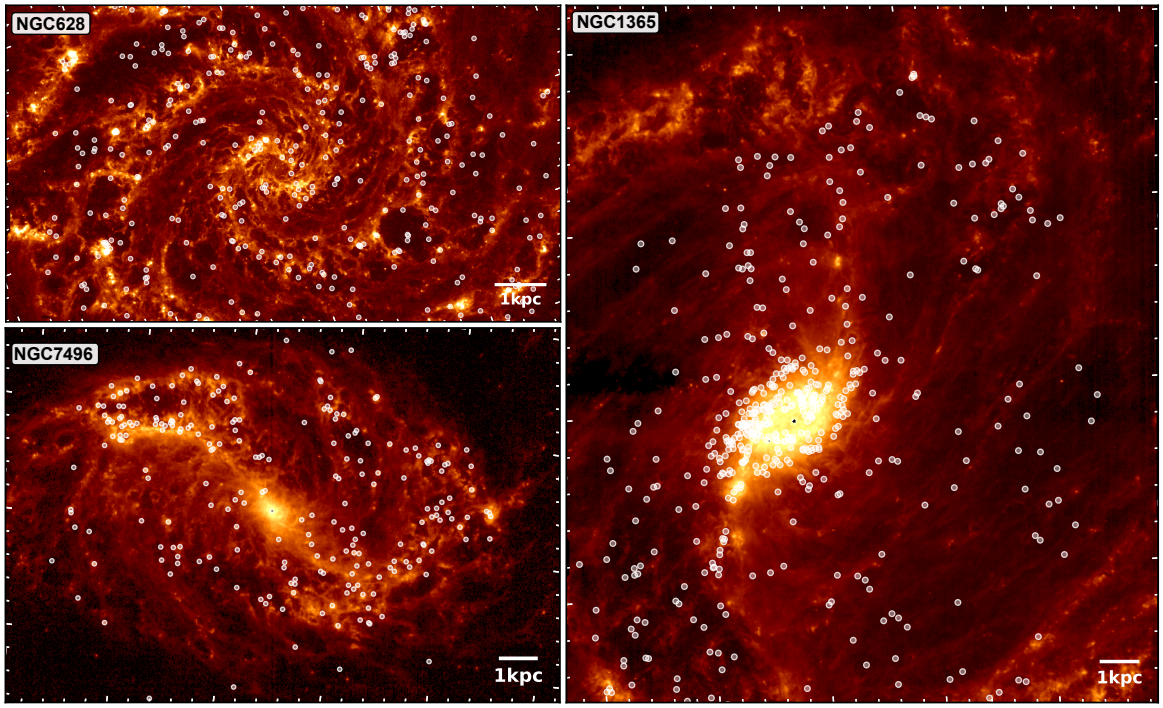


Figure 1. F770W imaging along with the locations of the stellar clusters. A 1 kpc scale bar is included within each panel.

et al. (2022), we reject sources that overlap with regions where the amplitude of the modeled PSFs, centered on the locations of the AGN, are $> 0.1\%$ of the PSF maxima. These masked central regions span 0.32 kpc^2 and 0.33 kpc^2, respectively, for NGC 1365 and NGC 7496. This step removes 6 clusters and 21 associations for NGC 1365 near the AGN, and 12 clusters and 33 associations for NGC 7496. If we further require a stellar mass of $\log(M_*/M_\odot) > 3.3$ to align with our targeted median cluster mass sensitivity for JWST observations (Lee et al. 2022b, Larson et al. in prep), then the cluster sample size drops another 5% and the association sample drops another 17%.

3. ANALYSIS

As described in Leroy et al. (2022), we first make small background level corrections to the imaging using galaxy-free regions in the outer portions of each image. Since our analysis relies on a combination of the F300M, F335M, F360M, F770W, and F1130W images, all the imaging was convolved with smoothing kernels following Aniano et al. (2011) to achieve the effective 0.″37 angular resolution of the F1130W data. Continuum-subtracted 3.3 μm PAH maps (F335M$_{\rm PAH}$) are constructed using the method outlined in Sandstrom et al. (2022) that leverages the F300M and F360M imaging to infer the underlying continua. No continuum subtraction is carried out for the F770W or F1130W imaging since the stellar contributions at these wavelengths are minor and the dust emission appearing in these two bands is dominated by PAH features (Smith et al. 2007; Egorov et al. 2022; Hassani et al. 2022). Future work will explore the impact of using, for example, the F1000W imaging as a proxy for the wavelength-adjacent continuum for the F770W and F1130W bands.

Aperture photometry is carried out for each compact stellar cluster using an aperture radius of 0.″3. The general trends discussed in § 4 are unaffected by modifications to our choice for aperture radius. The photometry for each stellar association is a simple sum of the fluxes for each pixel within the association's defined polygon, the edges for which are based on the surface 'brightness' of the smoothed tracer star maps (see Larson et al. 2023, in prep, for details). The choice of the 32 pc-scale stellar association watershed maps matches well with the apertures utilized for the compact stellar clusters—for our galaxy sample's distances, 0.″3 radii correspond to 14–28 pc. No local "background" subtraction is applied to the cluster or association photometry.

Draine et al. (2021) present various PAH band ratio diagrams for comparison with observations (e.g., see their Figures 16–21). Since the models of Draine et al. (2021) do not include contributions from stars, nebular lines, or other sources such as active galactic nuclei, in their analysis they employ a "clipping" method to focus solely on the PAH emission features. Because our observed photometry in the JWST bandpasses inevitably include contributions from such other non-PAH sources of emission, we make direct comparisons with the models by extracting synthetic fluxes for each bandpass using the CIGALE software (Boquien et al. 2019) and the Draine et al. (2021) models as the input simulated spectra. To simulate a variety of conditions we construct a suite of simulated spectra that span a range

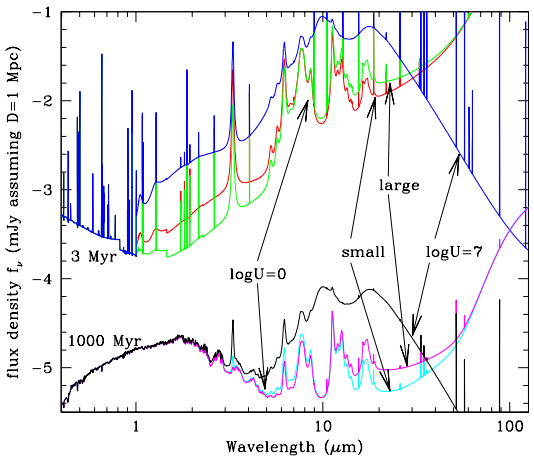


Figure 2. Example synthetic spectra drawn from the dust models of Draine et al. (2021) and generated using the CIGALE software (see § 3 for details). The spectra are shown for maximum differences in the chosen grid for stellar age, PAH size, and interstellar radiation field intensity. The changes in the spectra as a function of PAH ionization are less pronounced and are thus not displayed. The six different colors represent the six different example spectra, with their physical properties indicated by arrows and their descriptors.

of PAH ionizations (`ion` $= 0, 1, 2$; see Draine et al. 2021 Figure 9b), PAH size distributions (`size` $= 0, 1, 2$ corresponding to $a_{01} = 3, 4, 5$ Å; see Draine et al. 2021 Figure 9a), interstellar radiation field intensities U (`logU` $= 0 - 7$), and age of the main stellar population (`age` $= 3, 10, 100, 1000$ Myr). We assume solar metallicity Bruzual & Charlot (2003) stellar populations with a standard Chabrier (2003) initial mass function. Six of these synthetic spectra, chosen to demonstrate the dynamic range available in the models, are shown in Figure 2. The other parameters in CIGALE are fixed since varying them does not significantly change our results or interpretation, e.g., opting for an exponential star formation history with a late burst, solar metallicity, a Lyman continuum photon escape fraction of 0, etc. Finally, we have applied to our synthetic data the prescription outlined in Sandstrom et al. (2022) for removing the underlying continuum to the 3.3μm PAH feature emission, to be consistent with our treatment of the observations.

4. RESULTS AND DISCUSSION

Figure 3 provides the F335M$_{\rm PAH}$/F1130W and F335M$_{\rm PAH}$/F770W band ratios for the three galaxies, where we use the shorthand notation "F335M$_{\rm PAH}$" to represent νf_ν(F335M) for the PAH feature flux extracted for the F335M filter, etc. The data are color-coded according to stellar age. The two observed ratios each span about 1.4 dex, and they scale approximately linearly with each other; the numerators in the ratios are the same, and the denominators are comparable—thus the approximately one-to-one correlation seen in Figure 3. We provide in Table 1 the population medians and their semi-interquartile spreads in log base 10, along with the population means and their standard deviations. In addition, we provide the results of t-tests to quantify how significantly different are the population means. For the compact clusters in NGC 628 and NGC 7496 the medians and means for the F335M$_{\rm PAH}$/F1130W and F335M$_{\rm PAH}$/F770W ratios decrease with increasing stellar age as suggested by the synthetic model extractions described immediately below, particularly when comparing the <10 Myr and >100 Myr populations. For the stellar associations the overall distributions are consistent with what is observed for the compact clusters, and the older stellar populations show noticeably lower F335M$_{\rm PAH}$/F1130W and F335M$_{\rm PAH}$/F770W ratios in NGC 628 and NGC 1365. However, the t-test results imply that these differences are only statistically significant for the associations in NGC 628 and NGC 1365 and marginally significant for the clusters in NGC 628. Finally, we note that the scatter in the distributions increases with stellar age; the average semi-interquartile ranges for the young, intermediate, and old clusters and associations are 0.097, 0.122, and 0.124 dex and the average standard deviations are 0.216, 0.256, and 0.307 dex, respectively, for the three age populations.

We also include in Figure 3 the grid of synthetic points from the models of Draine et al. (2021) described in § 3. The magenta and blue grids in Figure 3 demonstrate how the synthetic points depend on stellar cluster age, PAH size distribution, and PAH ionization (after fixing $U = 1$). The black track portrays how the synthetic data vary with the intensity of the interstellar radiation field for $\log U = 0 - 7$ (after fixing `ion` $= 0$, `size` $= 2$, and `age` $= 10$ Myr). The large arrows and corresponding descriptors indicate how the synthetic tracks change with each modeled parameter; these synthetic trends are consistent with those portrayed in Figure 21d of Draine et al. (2021). The overall distributions of the observed ratios in Figure 3 track well with the displayed grid of synthetic models, and the majority of the observations are consistent with the PAHs having elevated ionization levels and large size distributions. In other words, the data are mostly populating the magenta grid for larger PAHs (and not the blue grid for smaller PAHs), between the magenta model tracks for 100 Myr and 1000 Myr, and the data are more closely aligned with the lefthand edge of the magenta grid that indicates more highly ionized PAHs. The implication is that the proximity of stellar clusters and associations has enhanced the photoejection of electrons from the PAHs.

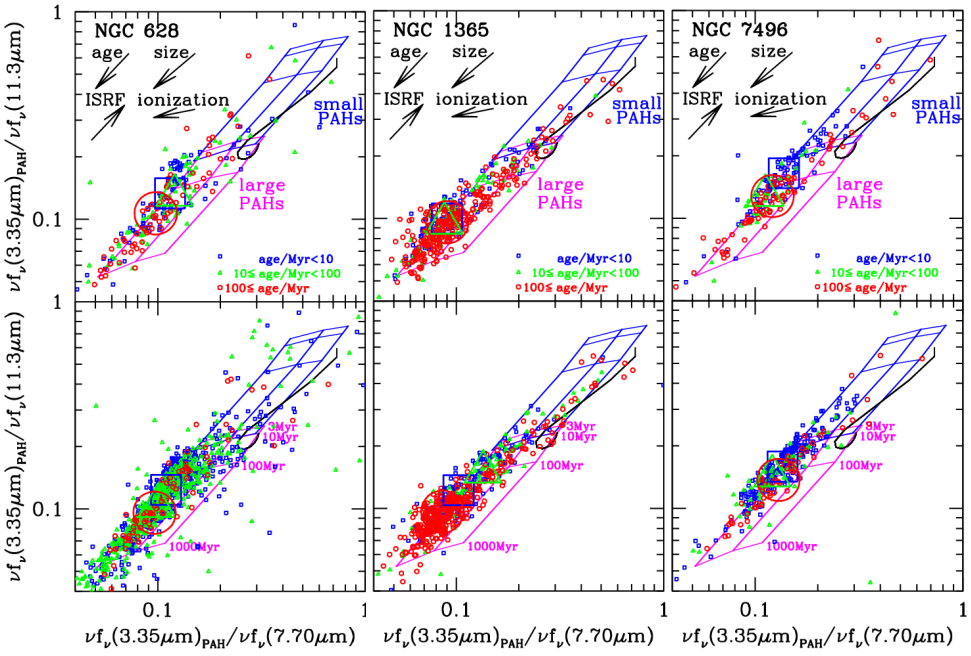


Figure 3. PAH bandpass flux ratios for the compact clusters (top) and stellar associations (bottom). The open blue squares, green triangles, and red circles are for compact stellar clusters, colored according to their ages: 0–10 Myr, 10–100 Myr, and >100 Myr, respectively. Large symbols indicate medians. Overlaid tracks are presented for select subsets of the simulated ratios, and the general trends for these tracks are indicated with the inset arrows/descriptions (see text for details). The magenta and blue tracks are for small (a_{01} = 3 Å) and large (a_{01} = 5 Å) modeled PAH distributions, respectively, with both assuming `logU`=0, `ion`=0,1.2, and `age`=10 Myr. The black hook-shaped track spans log U=0,7 and fixes `ion`=0, `size`=2, and `age`=10 Myr.

Table 1. Statistics for Figure 3

Galaxy	Population	age/Myr<10		10≤age/Myr<100		100≤age/Myr		probability
		†med$_x$,med$_y$	SIQR$_x$,SIQR$_y$	med$_x$,med$_y$	SIQR$_x$,SIQR$_y$	med$_x$,med$_y$	SIQR$_x$,SIQR$_y$	Kolm-Smir
NGC0628	clusters	−0.94,−0.88	0.08,0.13	−0.92,−0.88	0.12,0.15	−1.01,−0.97	0.15,0.17	$7{\cdot}10^{-3}$
NGC0628	associations	−0.96,−0.91	0.09,0.12	−1.00,−0.99	0.13,0.15	−1.02,−1.02	0.14,0.16	$2{\cdot}10^{-4}$
NGC1365	clusters	−1.05,−1.00	0.08,0.08	−1.06,−1.02	0.12,0.14	−1.04,−1.02	0.11,0.10	$1{\cdot}10^{-3}$
NGC1365	associations	−0.99,−0.91	0.11,0.12	−0.87,−0.82	0.14,0.13	−1.07,−1.02	0.09,0.07	$6{\cdot}10^{-8}$
NGC7496	clusters	−0.86,−0.78	0.09,0.10	−0.95,−0.89	0.09,0.09	−0.92,−0.89	0.15,0.14	$6{\cdot}10^{-4}$
NGC7496	associations	−0.87,−0.80	0.08,0.09	−0.92,−0.84	0.12,0.09	−0.89,−0.86	0.10,0.12	$6{\cdot}10^{-3}$
		‡mean$_x$,mean$_y$	σ_x,σ_y	mean$_x$,mean$_y$	σ_x,σ_y	mean$_x$,mean$_y$	σ_x,σ_y	t-test
NGC0628	clusters	−0.94,−0.89	0.22,0.24	−0.88,−0.86	0.35,0.27	−1.01,−0.97	0.36,0.37	0.16,0.10
NGC0628	associations	−0.96,−0.94	0.26,0.27	−1.00,−1.00	0.29,0.30	−1.03,−1.02	0.44,0.45	0.07,0.04
NGC1365	clusters	−1.02,−0.98	0.20,0.20	−1.02,−1.00	0.27,0.28	−0.99,−1.00	0.26,0.24	0.11,0.70
NGC1365	associations	−0.94,−0.90	0.22,0.22	−0.87,−0.85	0.27,0.25	−1.02,−1.00	0.26,0.26	0.03,0.0009
NGC7496	clusters	−0.89,−0.81	0.20,0.22	−0.96,−0.91	0.18,0.20	−0.85,−0.86	0.32,0.26	0.33,0.25
NGC7496	associations	−0.88,−0.81	0.17,0.18	−0.89,−0.86	0.20,0.22	−0.84,−0.82	0.23,0.23	0.26,0.63

†med$_x$ and med$_y$ refer to the medians of $\log_{10}$(F335M$_{\rm PAH}$/F770W) and $\log_{10}$(F335M$_{\rm PAH}$/F1130W), respectively. The semi-interquartile ranges are half the 25%–75% range found after sorting the flux ratios. The SIQRs provided here are in units of dex since they are computed using the (base 10) logarithms of the flux ratios. The Kolmogorov-Smirnov probabilities characterize how significantly the <10 Myr and >100 Myr two-dimensional distributions differ, with probabilities less than $\sim$ 0.05 indicating a significant difference (Press 1993).

‡mean$_x$ and mean$_y$ refer to the means of $\log_{10}$(F335M$_{\rm PAH}$/F770W) and $\log_{10}$(F335M$_{\rm PAH}$/F1130W), respectively; σ indicates the standard deviation. t-test probabilities characterize how significantly the <10 Myr and >100 Myr (one-dimensional log$x$,log$y$) means differ, with probabilities less than $\sim$ 0.05 indicating significantly different values (Press 1993).

Our evidence for higher levels of PAH ionization is conceptually consistent with the work of other PHANGS–JWST efforts appearing in this issue. Egorov et al. (2022) analyze the F1130W/F770W parameter, widely considered to be a tracer of the ratio of neutral to ionized PAHs (Draine & Li 2001; Maragkoudakis et al. 2020), in HII regions in NGC 628, NGC 1365, NGC 7496, and IC 5332 and find lower values of F1130W/F770W in regions with higher [S III]/[S II] ratios, indicating harder radiation fields. Chastenet et al. (2022) probe PAH band ratios across the disks of the four galaxies and find evidence of hotter, highly ionized PAHS in the vicinity of H II regions which are defined by the radiation from young stars. Finally, Sandstrom et al. (2022) create maps of PAH band ratios in the same three galaxies considered in this work and find fairly flat F335M$_{\rm PAH}$/F1130W radial profiles, with amplitudes similar to what we find (0.07–0.24 in νf_ν units). A follow-up control study using a larger sample of PHANGS galaxies will compare the PAH ionization levels inferred in this work near stellar clusters and associations with those of PAHs that are spread throughout the diffuse interstellar medium.

Close scrutiny of Figure 3 suggests subtle differences between galaxies, such as the sources in NGC 7496 being on average higher up in the magenta grid which is consistent with more intense radiation fields (and/or young stellar ages). It is unlikely that the AGN in NGC 7496 is responsible for this difference, as we have removed the central clusters and associations from our analysis (see § 2) and our stellar sources in NGC 7496 are dispersed throughout its disk and spiral arms (Figure 1). In addition, NGC 628 shows larger scatter in the data than for NGC 1365 and NGC 7496, with standard deviations in the abscissa and ordinate values larger by a factor of 1.23, 1.30, and 1.56 for the <10 Myr, 10–100 Myr, and >100 Myr populations, respectively. The factor of two larger distances for NGC 1365 and NGC 7496 compared to the distance for NGC 628 result in more spatial averaging over the 0.″6 diameter aperture and thus the smaller scatter in the data.

5. CONCLUSIONS

We have leveraged new JWST near- and mid-infrared imaging of NGC 628, NGC 1365, and NGC 7496 to study their PAH emission. With the combined data from the three galaxies we are able to analyze the PAH emission over localized (< 32 pc scale) regions centered on 1063 compact stellar clusters and 2654 stellar associations previously analyzed with HST ultraviolet/optical imaging. This study represents the first look at matched PAH band ratios, at high angular resolution, for large statistical samples of stellar ionizing sources isolated from more diffuse ISM conditions, enabling us to directly link ionizing sources to their impact on PAH properties across representative disk environments.

To enable a comparison with theoretical expectations, we extracted synthetic infrared colors based on models of stellar, PAH, and dust continuum emission. A full grid of synthetic values is created by modifying four key parameters: stellar age, PAH ionization fraction, PAH size distribution, and interstellar radiation field intensity. Our results are generally consistent with the predictions from the dust models outlined in Draine et al. (2021), though the PAH band ratios we measure for the youngest stellar clusters and associations (< 10 Myr) appear between theoretical grid values (assuming large PAH size distributions) for stellar ages between 100 Myr and 1000 Myr. In addition, we find statistical evidence for the stellar associations in NGC 628 and NGC 1365 having decreasing values of F335M$_{\rm PAH}$/F1130W and F335M$_{\rm PAH}$/F770W with increasing stellar age, consistent with the expectations based on the synthetic extractions. The slope and the overall distribution for the ensemble of synthetic PAH band ratios is consistent with that for the observed distributions in the three galaxies, and the models with higher levels of PAH ionization and larger size distributions are generally more aligned with the observations. A higher level of ionization could indicate enhanced processing of PAHs from the radiation fields produced by the stellar clusters. Finally, there is an age-dependent trend in the scatter, with older stellar populations exhibiting larger dispersions in the PAH band ratios.

Further additional analysis with the full PHANGS–JWST sample is needed to more firmly test theoretical dust models. The larger PHANGS sample will enable us to explore PAH band ratios as a function of local metallicity and radiation hardness indicators, and thus bring additional insight into the dearth of PAHs for environments of depressed metal abundance and/or elevated radiation hardness. Furthermore, an analysis that leverages the larger PHANGS-JWST sample will provide a more robust control sample for measuring PAH band ratios in diffuse regions as a control sample against which we will compare our measurements near stellar clusters and associations.

6. ACKNOWLEDGMENTS

We thank the referee for their thoughtful review. This work is based on observations made with the NASA/ESA/CSA JWST and Hubble Space Telescopes. The data were obtained from the Mikulski Archive for Space Telescopes at the Space Telescope Science Institute, which is operated by the Association of Universities for Research in Astronomy, Inc., under NASA contract NAS 5-03127 for JWST and NASA contract NAS 5-26555 for HST. The JWST observations are associated with Program 2107, and those from HST with Program 15454. The specific observations analyzed can be accessed via 10.17909/9bdf-jn24. The HST images and catalogs can be access via 10.17909/t9-r08f-dq31 and 10.17909/jray-9798, respectively. FB

would like to acknowledge funding from the European Research Council (ERC) under the European Union's Horizon 2020 research and innovation programme (grant agreement No.726384/Empire). MB acknowledges support from FONDECYT regular grant 1211000 and by the ANID BASAL project FB210003. JC acknowledges support from ERC starting grant #851622 DustOrigin. MC gratefully acknowledges funding from the Deutsche Forschungsgemeinschaft (DFG) through an Emmy Noether Research Group (grant number CH2137/1-1). KG is supported by the Australian Research Council through the Discovery Early Career Researcher Award (DECRA) Fellowship DE220100766 funded by the Australian Government. KG is supported by the Australian Research Council Centre of Excellence for All Sky Astrophysics in 3 Dimensions (ASTRO 3D), through project number CE170100013. JMDK gratefully acknowledges funding from the European Research Council (ERC) under the European Union's Horizon 2020 research and innovation programme via the ERC Starting Grant MUSTANG (grant agreement number 714907). COOL Research DAO is a Decentralized Autonomous Organization supporting research in astrophysics aimed at uncovering our cosmic origins. KK, OE gratefully acknowledge funding from the Deutsche Forschungsgemeinschaft (DFG, German Research Foundation) in the form of an Emmy Noether Research Group (grant number KR4598/2-1, PI Kreckel). RSK acknowledges financial support from the European Research Council via the ERC Synergy Grant "ECOGAL" (project ID 855130), from the Deutsche Forschungsgemeinschaft (DFG) via the Collaborative Research Center "The Milky Way System" (SFB 881—funding ID 138713538—subprojects A1, B1, B2 and B8) and from the Heidelberg Cluster of Excellence (EXC 2181—390900948) "STRUCTURES", funded by the German Excellence Strategy. RSK also thanks the German Ministry for Economic Affairs and Climate Action for funding in the project "MAINN" (funding ID 50OO2206). AKL gratefully acknowledges support by grants 1653300 and 2205628 from the National Science Foundation, by award JWST-GO-02107.009-A, and by a Humboldt Research Award from the Alexander von Humboldt Foundation. ER acknowledges the support of the Natural Sciences and Engineering Research Council of Canada (NSERC), funding reference number RGPIN-2022-03499. EJW acknowledges the funding provided by the Deutsche Forschungsgemeinschaft (DFG, German Research Foundation) – Project-ID 138713538 – SFB 881 ("The Milky Way System", subproject P1). TGW acknowledges funding from the European Research Council (ERC) under the European Union's Horizon 2020 research and innovation programme (grant agreement No. 694343).

REFERENCES

Allamandola, L. J., Hudgins, D. M., & Sandford, S. A. 1999, ApJL, 511, L115

Anand, G. S., Lee, J. C., Van Dyk, S. D., et al. 2021a, MNRAS, 501, 3621

Anand, G. S., Rizzi, L., Tully, R. B., et al. 2021b, AJ, 162, 80

Aniano, G., Draine, B. T., Gordon, K. D., & Sandstrom, K. 2011, PASP, 123, 1218

Aniano, G., Draine, B. T., Hunt, L. K., et al. 2020, ApJ, 889, 150

Boquien, M., Burgarella, D., Roehlly, Y., et al. 2019, A&A, 622, A103

Bruzual, G., & Charlot, S. 2003, MNRAS, 344, 1000

Chabrier, G. 2003, PASP, 115, 763

Chastenet, J., Leroy, A., & Schinnerer, E. 2022, ApJL

Chastenet, J., Sandstrom, K., Chiang, I.-D., et al. 2019, ApJ, 876, 62

Dale, D. A., Cohen, S. A., Johnson, L. C., et al. 2009, ApJ, 703, 517

DeFrees, D. J., & Miller, M. D. 1989, in Interstellar Dust, ed. L. J. Allamandola & A. G. G. M. Tielens, Vol. 135, 173–176

Deger, S., Lee, J. C., Whitmore, B. C., et al. 2022, MNRAS, 510, 32

Draine, B. T., & Li, A. 2001, ApJ, 551, 807

Draine, B. T., Li, A., Hensley, B. S., et al. 2021, ApJ, 917, 3

Draine, B. T., Dale, D. A., Bendo, G., et al. 2007, ApJ, 663, 866

Egorov, D., Leroy, A., & Schinnerer, E. 2022, ApJL

Emsellem, E., Schinnerer, E., Santoro, F., et al. 2022, A&A, 659, A191

Engelbracht, C. W., Gordon, K. D., Rieke, G. H., et al. 2005, ApJL, 628, L29

Engelbracht, C. W., Rieke, G. H., Gordon, K. D., et al. 2008, ApJ, 678, 804

Galliano, F., Nersesian, A., Bianchi, S., et al. 2021, A&A, 649, A18

Hassani, H., Leroy, A., & Schinnerer, E. 2022, ApJL

Hollenbach, D. J., & Tielens, A. G. G. M. 1997, ARA&A, 35, 179

Jensen, J. J., Hönig, S. F., Rakshit, S., et al. 2017, MNRAS, 470, 3071

Kourkchi, E., & Tully, R. B. 2017, ApJ, 843, 16

Lai, T. S. Y., Smith, J. D. T., Baba, S., Spoon, H. W. W., & Imanishi, M. 2020, ApJ, 905, 55

Lee, J., Leroy, A., & Schinnerer, E. 2022a, ApJL

Lee, J. C., Whitmore, B. C., Thilker, D. A., et al. 2022b, ApJS, 258, 10
Leroy, A., Schinnerer, E., & Rosolowsky, E. 2022, ApJL
Leroy, A. K., Schinnerer, E., Hughes, A., et al. 2021, ApJS, 257, 43
Madden, S. C., Galliano, F., Jones, A. P., & Sauvage, M. 2006, A&A, 446, 877
Maragkoudakis, A., Peeters, E., & Ricca, A. 2020, MNRAS, 494, 642
Press, W. H. 1993, Science, 259, 1931
Rémy-Ruyer, A., Madden, S. C., Galliano, F., et al. 2015, A&A, 582, A121
Riechers, D. A., Pope, A., Daddi, E., et al. 2014, ApJ, 786, 31
Rieke, G. H., Wright, G. S., Böker, T., et al. 2015, PASP, 127, 584
Rieke, M. J., Kelly, D., & Horner, S. 2005, in Society of Photo-Optical Instrumentation Engineers (SPIE) Conference Series, Vol. 5904, Cryogenic Optical Systems and Instruments XI, ed. J. B. Heaney & L. G. Burriesci, 1–8
Rigopoulou, D., Barale, M., Clary, D. C., et al. 2021, MNRAS, 504, 5287
Sandstrom, K., Leroy, A., & Schinnerer, E. 2022, ApJL
Sandstrom, K. M., Bolatto, A. D., Draine, B. T., Bot, C., & Stanimirović, S. 2010, ApJ, 715, 701
Shaya, E. J., Tully, R. B., Hoffman, Y., & Pomarède, D. 2017, ApJ, 850, 207
Smith, J. D. T., Draine, B. T., Dale, D. A., et al. 2007, ApJ, 656, 770
Thilker, D. A., Whitmore, B. C., Lee, J. C., et al. 2022, MNRAS, 509, 4094
Tielens, A. G. G. M. 2008, ARA&A, 46, 289
Turner, J. A., Dale, D. A., Lee, J. C., et al. 2021, MNRAS, 502, 1366
Whitmore, B. C., Lee, J. C., Chandar, R., et al. 2021, MNRAS, 506, 5294
Wolfire, M. G., Vallini, L., & Chevance, M. 2022, ARA&A, 60, 247
Wu, Y., Charmandaris, V., Hao, L., et al. 2006, ApJ, 639, 157
Wu, Y., Helou, G., Armus, L., et al. 2010, ApJ, 723, 895